Lightweight and Construable Magnetic Wood for Electromagnetic Interference Shielding

Zheng Cheng, Yuyi Wei, Chao Liu, Yong Chen, Yi Ma, Huaihao Chen, Xianfeng Liang, Nian X. Sun,* and Hongli Zhu*

Currently, due to the rapid development of communication technology, electromagnetic interference (EMI) and irradiation have become an emerging environmental pollutant. Herein, hierarchical and porous structured wood is used as the lightweight three-dimensional organic scaffold for the incorporation of magnetic iron oxide nanoparticles through an in situ mineralization process that endows the woodblock with favorable appearance as well as magnetic and EMI shielding properties. The two-step process involves the removal of lignin from natural wood via cooking and bleaching followed by inorganic mineralization. The resultant magnetic wood displays an optical brown appearance and possesses a typical magnetic hysteresis behavior with a saturation magnetization of 4.5 emu g⁻¹ for the whole wood. More importantly, the obtained magnetic wood is much lighter than traditional magnetic metal and construable for versatile applications. Notably, the 3 mm thick magnetic wood shows 5-10 dB (or 7-10×) enhanced electromagnetic wave attenuation across the X-band of 8-12 GHz compared with nonmagnetic wood with the same thickness. The enhanced electromagnetic wave absorption of magnetic wood is mainly due to its enhanced magnetic loss tangent compared with nonmagnetic wood. This work provides an inspiring strategy to develop sustainable, lightweight, and environmentally friendly wood for multifunctional magnetic applications.

Currently, booming telecom technology and digital systems bring convenience to human life and generate a large amount of electromagnetic interference (EMI), which not only affects information security but also causes harmful electromagnetic radiation pollution. To address these electromagnetic pollution problems, various EMI shielding materials have been developed. Among them, iron oxide, a typical magneto-dielectric material with both magnetic loss and dielectric loss, is one of

Dr. Z. Cheng, Dr. C. Liu, Dr. Y. Chen, Dr. Y. Ma, Prof. H. Zhu Department of Mechanical and Industrial Engineering

Northeastern University Boston, MA 02115, USA E-mail: h.zhu@neu.edu

Dr. Y. Wei, Dr. H. Chen, Dr. X. Liang, Prof. N. X. Sun Electric and Computer Engineering Department Northeastern University

Boston, MA 02115, USA E-mail: n.sun@neu.edu

The ORCID identification number(s) for the author(s) of this article can be found under https://doi.org/10.1002/adem.202000257.

DOI: 10.1002/adem.202000257

the most attractive microwave-absorbing materials. [5] However, limitations on the direct application of magneto-dielectric materials or conventional metal-based materials in EMI shielding fields still exist due to high density, high material thickness, fabrication difficulty, and unsatisfactory shielding effectiveness. [6,7] Thus, the development of ideal EMI shielding materials that are lightweight, construable, and thermally stable and have strong absorption capacities is essential and urgently needed.

Wood is a natural lightweight composite that has excellent mechanical properties and unique mesostructures resulting from its natural growth. One of the best features of wood is its structural anisotropy with vertically aligned channels, which are used to pump ions, water, and other ingredients through the wood trunk to meet its metabolic needs. Recently, different approaches for the modification and functionalization of wood have been studied to improve wood quality and raise its added value. Hu and co-workers utilized natural wood to fabricate func-

tional transparent wood composites that exhibit extraordinary anisotropic optical and mechanical properties.^[11] Yu et al. reported a simple strategy for the large-scale fabrication of artificial polymeric woods with outstanding performance, including mechanical strength comparable to that of natural wood, preferable corrosion resistance to water and acid with no decrease in the mechanical properties, as well as excellent thermal insulation and fire retardancy.^[12] Yuan et al. prepared a stiff, thermally stable, and highly anisotropic carbonized wood composite with EMI shielding effectiveness by incorporating silver nanowires (AgNWs).^[13] Although the carbon composite is lightweight with good EMI shielding performance, AgNWs are expensive, and a high loading of AgNWs would result in complicated processing, large amounts of agglomerates, and poor mechanical strength.

For general application, wood materials usually need preservation and coloring, where the coloration is typically obtained by impregnating wood with organic pigments or coating wood sheets with toxic and volatile organic varnish. [14] These solutions are ineffective when exposed to UV radiation or heating. With the development of state-of-art techniques, iron oxide pigment has become the second most used inorganic pigment, and it includes multiple colors, such as iron oxide red, iron oxide yellow, iron

www.advancedsciencenews.com www.aem-journal.com

oxide brown, and iron oxide black. In particular, iron oxide brown is widely used as a typical brown pigment. [15] Iron oxide can be well utilized, because wood can be mineralized to create hierarchically structured organic-inorganic hybrid materials with novel properties. Furthermore, the literature has demonstrated that mineralized wood benefits from the structural integrity of natural wood, which has hierarchical pores that are beneficial to the deposition of inorganic minerals.^[16] Different colors can be produced by the presence of goethite in petrified wood, and the intensity of the color depends on the quantity of iron-containing minerals.[17]

Herein, we report the fabrication of magnetic wood based on the in situ deposition of magnetic Fe₃O₄ nanoparticles into a delignified wood template through an inorganic mineralization method. The morphology, microstructure, chemical components, and magnetic characteristics of the obtained wood samples were investigated. The original structure of the wood was well preserved. The EMI shielding effect of magnetic wood with wood-ferrite multilayers was studied, and adequate signal strength attenuation was observed by applying magnetic wood as a shield during the test. A series of tests using air, natural wood, and delignified wood as control groups for EMI shielding effect studies were carried out, and magnetic wood was shown to be very effective across the X-band of 8-12 GHz. The study indicates that the magnetic wood is a promising candidate for various applications, such as the green shielding material in construction, furniture, decoration, packing, etc.

In this work, inspired by the unique structure of natural wood, magnetic wood with an optical brown appearance and an excellent EMI shielding property was fabricated via the lignin removal followed by an inorganic mineralization process, as shown in Figure 1. In general, there are three primary chemical components in the trees: cellulose, hemicellulose, and lignin (Figure 1a).[18] Among them, lignin provides the rigidity and brown color of natural wood (Figure 1b).[19] After lignin is removed, the wood (referred as delignified wood in Figure 1c) becomes soft and white, and micro- to nanosized pores in the wood are opened. [20] Then, darker brown magnetic wood can be obtained through an inorganic mineralization process (Figure 1d). Notably, assembling smaller magnetic wood blocks into a larger wooden model is readily achievable and crucial for industrial applications (Figure 1e). Benefiting from the magnetic Fe₃O₄ nanoparticles deposited on the interconnected porous network structured wood substrate, the wood-derived magnetic materials are expected to exhibit excellent EMI shielding performance. The shielding property is due to the distinctive selfassembling anisotropic morphology of Fe₃O₄ nanoparticles formed on the inner surface of the wood lumen walls, which leads to the construction of a wood-ferrite multilayer structure. This multilayer structure can provide large magnetic loss

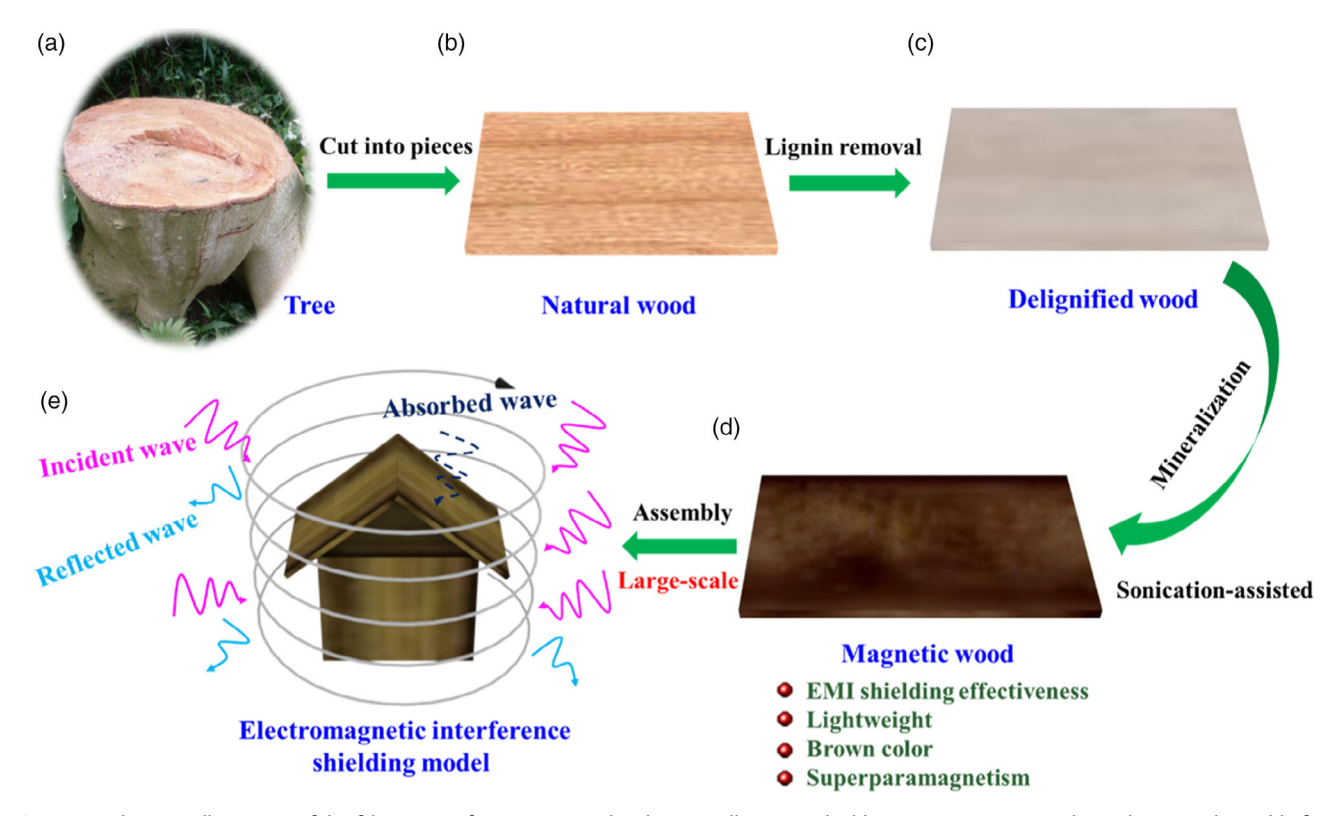


Figure 1. Schematic illustration of the fabrication of magnetic wood with an excellent EMI shielding property. a) Natural tree. b) Natural wood before delignification. c) Delignified wood via the cooking and bleaching process for the lignin removal. d) Magnetic wood obtained from the inorganic mineralization process. e) Schematic of the EMI shielding effect of the lightweight magnetic wood model, which is assembled with smaller individual magnetic wood blocks for scalable practical application. As the electromagnetic incident waves (pink arrows) strike the surface of the magnetic wood, some waves are immediately reflected (atrovirens arrows), and some waves are absorbed (dark blue dotted arrow).

ENGINEERING

www.advancedsciencenews.com www.aem-journal.com

tangent, optimal impedance matching, and an interconnected 3D network for electromagnetic wave absorption, reflection, and attenuation.[3,21]

At the start of the fabrication process, wood slices with a thickness of 3 mm were obtained by cutting a basswood block along the radial direction (tree growth direction) (Figure S1, Supporting Information), and these slices were then used as the basic material for magnetic wood preparation. The natural wood has a pale yellow color due to the light absorption capability of lignin. We first used the facile two-step process to remove the lignin from natural wood. Wood slices were soaked in a boiling solution containing NaOH and Na2SO3 (cooking process, Figure 2a-c) to dissolve part of the lignin content, which is a common chemical process used in the pulping industry. Then, the wood slices were transferred into a boiling H2O2 solution (Figure S2, Supporting Information) to further remove the remaining lignin (bleaching process, Figure 2d-f). The color in the wood slices can be used to indicate the amount of lignin presented in the bulk surface of the wood, because lignin is colored and cellulose is colorless. After delignification, the wood slice becomes light white, demonstrating the successful lignin removal (Figure S3, Supporting Information). A color comparison of the wood slices before and after bleaching is shown in Figure S4, Supporting Information, illustrating that the light can pass through the delignified wood, and thus, the delignified

wood exhibits certain transmittance. The process of obtaining the delignified wood is simple, which means fabricating a large amount of wood pieces at the same time is applicable in industry. Magnetic wood was then produced via an inorganic mineralization process, which is entailed on alternating incubation cycles with 0.5 mol L⁻¹ FeSO₄ and Na₂CO₃ solutions assisted by moderate sonication (Figure 2h,i). [22]

The morphology and microstructure of natural wood, delignified wood, and magnetic wood were also systematically investigated. As shown in Figure 3a,d, the vertically aligned fiber tracheids and large-lumen vessels can be clearly seen in the axial plains of the pale vellow natural wood. The wood cell wall is comprised mainly of cellulose, hemicelluloses, and lignin, and they intertwine with each other to provide the necessary mechanical integrity to the bulk wood. Such three-dimensional (3D) hierarchical wood scaffold with special structural anisotropy shows great potential for further functionalization. The magnified scanning electron microscopy (SEM) image also shows the smaller pits on the inner surface of the lumen (Figure 3e), representing the secondary pores. These secondary pores enable material transport in the axial direction of the wood trunk.[11] Figure 3b shows a photograph of the delignified wood block after the lignin removal. The yellowish wood block becomes white after delignification, indicating the successful removal of dark-colored lignin, whereas the colorless polysaccharides are left behind.

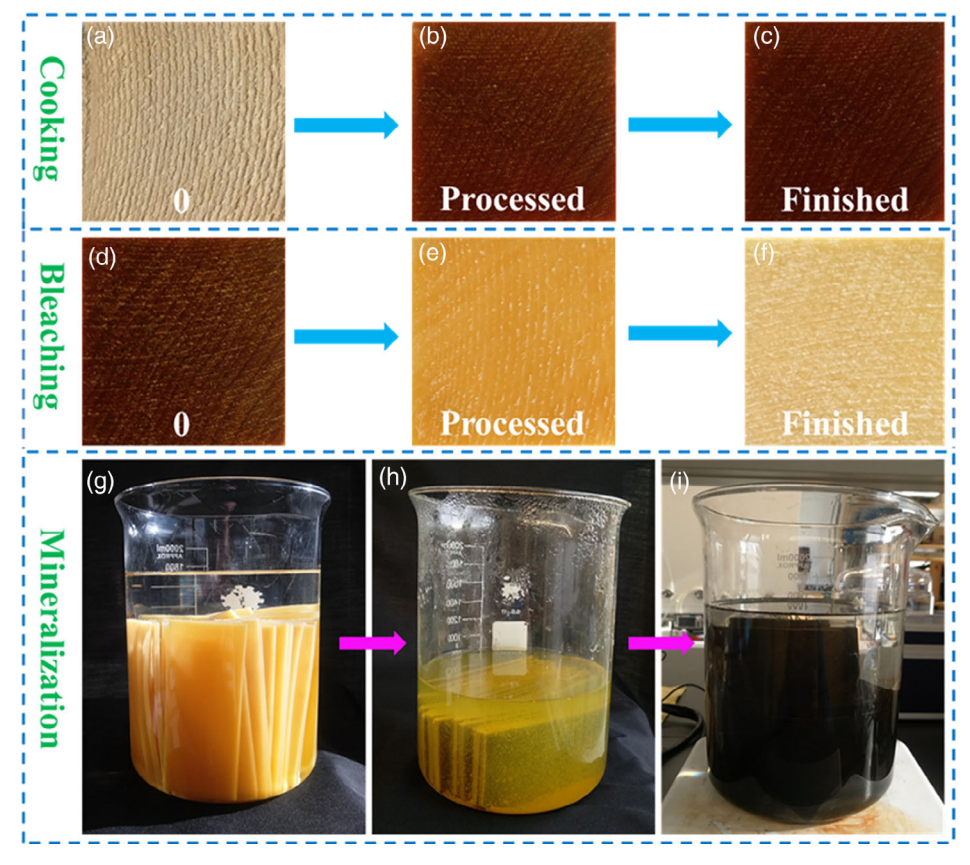


Figure 2. Fabrication process of magnetic wood with a thickness of 3 mm. a-c) Comparison of color changes of basswood during the cooking process. d-f) Comparison of color changes of wood during the bleaching process. g) The delignified wood slice immersed in DI water. h) The clean wood slices were inorganically mineralized by performing alternating incubation cycles with 0.5 mol L-1 FeSO₄ and 0.5 mol L-1 Na₂CO₃ solutions. i) The magnetic wood slices were washed with DI water at least three times.

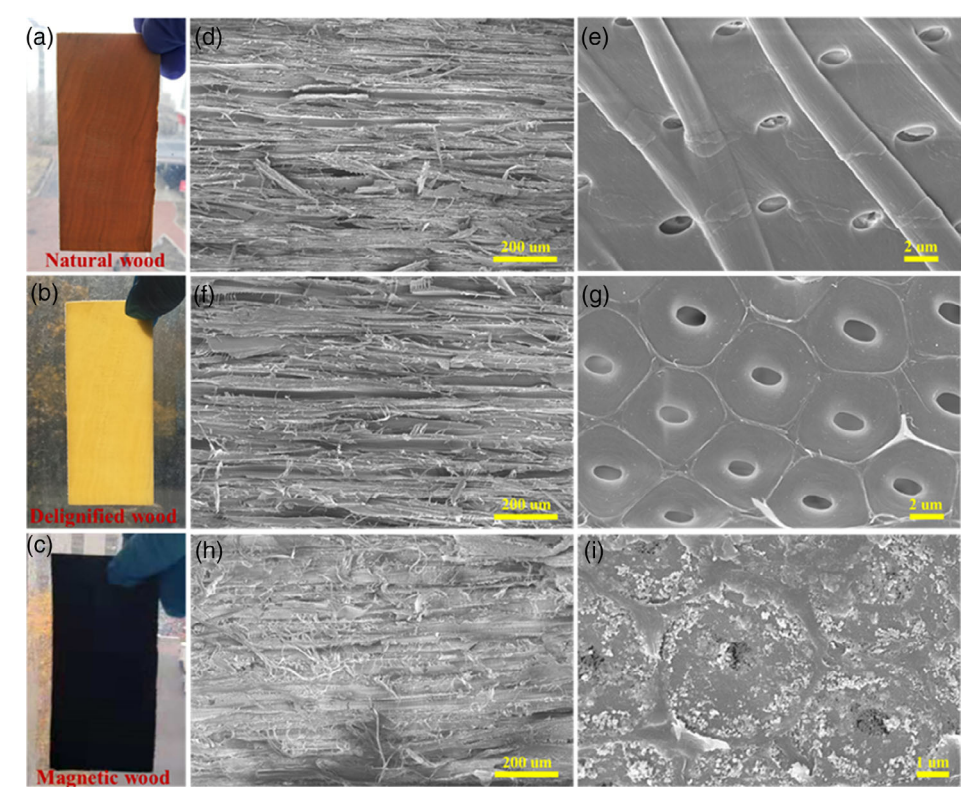


Figure 3. Morphology and microstructure of different wood samples. a) Photograph of the natural wood. b) Photograph of the delignified wood. c) Photograph of the magnetic wood. d) Axial direction (wood growth direction) SEM image of the natural wood, showing the alignment of the microchannels. e) High-magnification axial direction SEM image of the natural wood, in which some secondary pores are clearly seen. f) Axial direction SEM image of the delignified wood, exhibiting a loose and porous structure. g) High-magnification axial direction SEM image of the delignified wood, showing that the secondary pores became more open after the lignin removal. h) Axial direction SEM image of the magnetic wood, showing the nanosized iron oxide particles distributed inside the cell wall. i) High-magnification axial direction SEM image of the magnetic wood. The iron oxide nanoparticles covered the wood surface, and some were embedded in or were even blocking the secondary pores.

The delignification process also leads to significant changes in the morphology and microstructure of the wood block. The original compact cell wall evolved into a loosened skeleton with numerous pores generated in the wall, as shown in Figure 3f. However, the microstructure with well-defined channels was well preserved after the delignification process. The highmagnification SEM image further reveals the changes in the microstructure of the cell wall (Figure 3g), and it is noted that the small pores became more open after the lignin removal. Figure 3c shows magnetic wood obtained after the inorganic mineralization process, displaying an optical dark brown appearance. The axial direction SEM image revealed that the nanosized iron oxide particles were distributed inside the cell wall (Figure 3h). In the high-magnification SEM images, it was observed that the iron oxide nanoparticles uniformly covering the wood surface (Figure S5, Supporting Information), and some were embedded in or even blocking the secondary pores (Figure 3i). The nanosized iron oxide particles were generated from the chemical, hydrolysis, and oxidation reactions of FeSO₄ and Na₂CO₃ substance.

Figure 4a,b shows an optical brown appearance on both the surface as well as the cross section of the magnetic wood, further indicating that iron oxides nanoparticles are uniformly

distributed in the wood. In addition, corresponding elemental mapping images of oxygen (O), carbon (C), and iron (Fe) of the magnetic wood were obtained and are shown in Figure 4c-f. Based on the consistent distribution of Fe element in Figure 4f, we can further conclude that Fe was successfully incorporated into the delignified wood after the inorganic mineralization process. The presence of iron oxide was confirmed according to the results obtained from X-ray photoelectron spectroscopy (XPS) measurements, because core electron lines of ferrous and ferric ions are both detected and are distinguishable from each other in the XPS spectra (Figure 4g). The XPS spectra also verified that the natural wood and delignified wood contain mainly O and C, whereas the magnetic wood contains O, C, and Fe. For determination of the oxidation states of the elements, high-resolution XPS was conducted, and Fe 2p, O 1s, and C 1s spectra were obtained (Figure 4h and Figure S6, Supporting Information). As shown in Figure 4h, the binding energies at \approx 707 and \approx 722 eV were the characteristic doublets from Fe $2p_{3/2}$ and Fe $2p_{1/2}$ core-level electrons, confirming that the iron oxide present is Fe₃O₄. [3] Figure S6a, Supporting Information, displays the high-resolution XPS spectra of O 1s. Two characteristic peaks of O 1s were observed for magnetic wood. The peak at \approx 529.2 eV was attributed to the C 1s for

ENGINEERING
____ MATERIALS

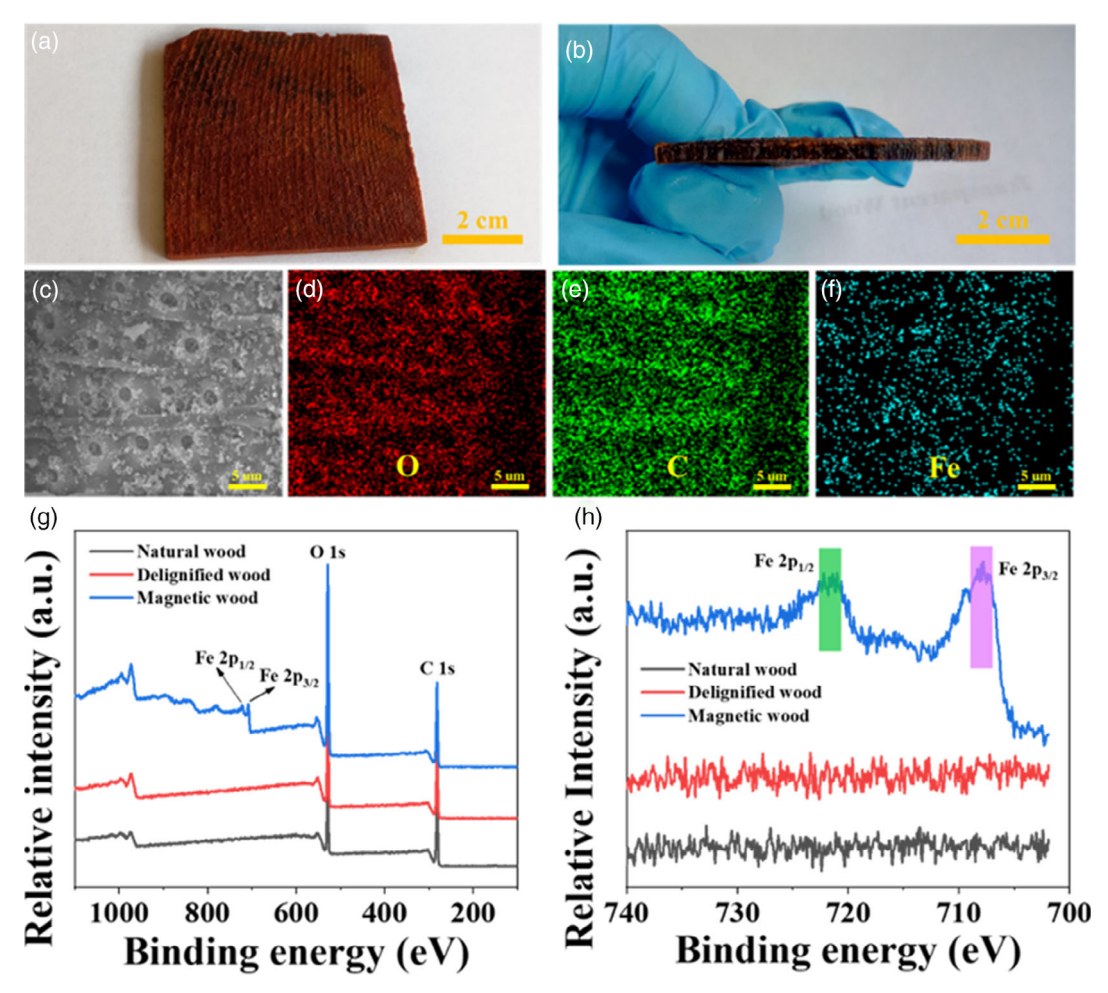


Figure 4. a) Photograph of the surface of the magnetic wood. b) Photograph of the cross section of the magnetic wood. c) SEM images of the magnetic wood. Elemental maps of the magnetic wood for d) oxygen, e) carbon, and f) iron. g) XPS spectra of natural wood, delignified wood, and magnetic wood. h) High-resolution Fe 2p spectra of natural wood, delignified wood, and magnetic wood.

carbohydrates, which was also observed in the natural wood. The peak at $\approx\!526.8\,eV$ was attributed to Fe $_3O_4$, which was absent in the natural wood and delignified wood. Figure S6b, Supporting Information, shows the high-resolution XPS spectra of C 1s, and two characteristic shoulder peaks were observed for natural wood, delignified wood, and magnetic wood.

Figure 5a shows the X-ray diffraction (XRD) patterns of the natural wood, delignified wood, and magnetic wood. Both natural wood and delignified wood display two primary diffraction peaks at 16.8° and 22.5° , which can be assigned to the (100) and (002) planes of cellulose, respectively. However, the characteristic peaks of cellulose were not obvious in the magnetic wood sample, which is attributed to the fact that iron oxide covers the wood substrate. The magnetic wood showed additional diffraction peaks at $2\theta = 30.2^{\circ}$, 35.6° , 43.2° , 53.6° , 57.1° , and 62.7° , corresponding to the (220), (311), (400), (422), (511), and (440) planes of Fe₃O₄ in a cubic phase. [23] Figure 5b shows the Fourier transform infrared (FTIR) spectra of the natural wood, delignified wood, and magnetic wood. The natural wood presented characteristic absorption peaks, including 3335 and 1642 cm⁻¹ (O—H stretching vibrations), 2920 cm⁻¹ (C—H stretching vibration)

1722 cm⁻¹ (C=O stretching vibrations), 1508 cm⁻¹ (the aromatic ring stretching vibrations of lignin), 1457 cm⁻¹ (C=O symmetric stretching vibrations), 1231 cm⁻¹ (aromatic C–H in-plane deformation assigned to lignin), and 1160 cm⁻¹ (C—O—C asymmetric stretching vibration), which is in agreement with the previous literature. [24-26] After the lignin removal, the bands at $\approx\!\!1508$ and 1231 cm⁻¹ became weaker or even disappeared, further indicating the degradation of light-absorbing lignin. When the Fe₃O₄ nanoparticles were added to the delignified wood, the stretching vibrations of Fe-O can be clearly seen at 576, 665, and $783\,\text{cm}^{-1}$. These results further confirm that the Fe₃O₄ nanoparticles were successfully deposited on the delignified wood. The introduction of magnetic Fe₃O₄ particles into the wood substrate was also indicated by thermogravimetric analysis (TGA), as shown in Figure 5c,d. The simultaneous thermal analysis of natural wood, delignified wood, and magnetic wood was carried out under a nitrogen atmosphere. Two stages of mass loss were observed in the natural wood and delignified wood. The first stage at approximately 100 °C was due to the elimination of moisture, and the major mass loss of the natural wood in the range of 260-390 °C was caused by the pyrolysis of wood components,

ENGINFERING

www.advancedsciencenews.com

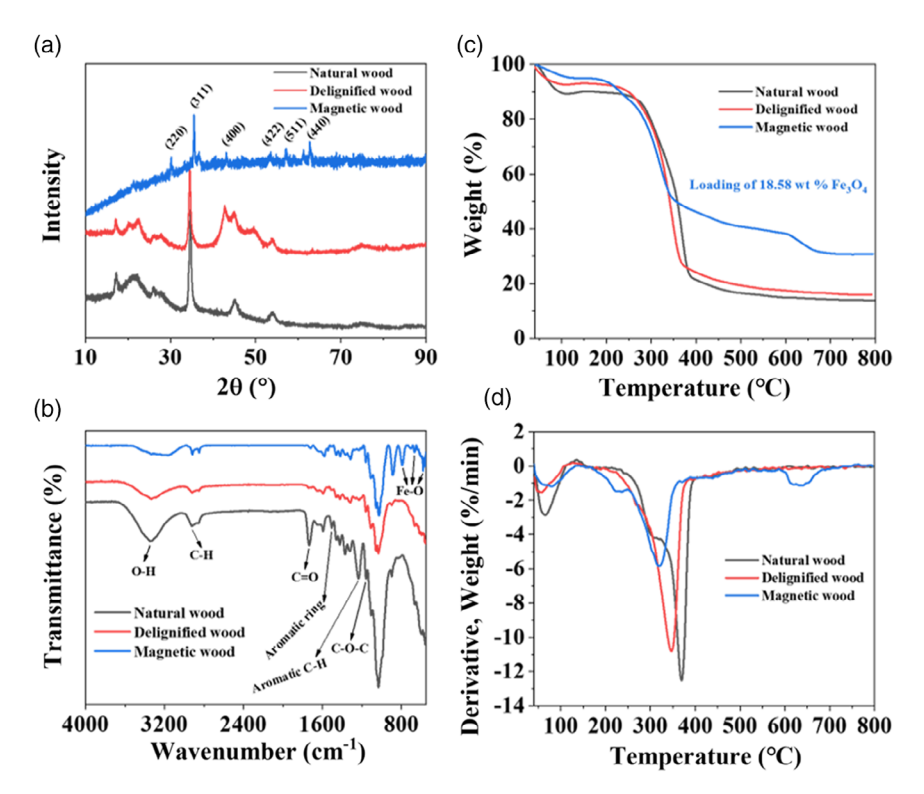


Figure 5. a) XRD patterns, b) FTIR spectra, c) TG curves, and d) DTG curves of natural wood, delignified wood, and magnetic wood. The magnetic wood contains 18.58 wt% Fe₃O₄ nanoparticles.

including cellulose, hemicellulose, and lignin. The fact that 12.67 wt% residue mass remained after heating to 600 °C and no further mass loss occurred when the temperature was increased to 800 °C suggests that the wood was converted to charcoal under the experimental temperature conditions. [28] The major mass loss of the delignified wood occurred between 230 and 370 °C, which is slightly lower than natural wood due to the removal of lignin. However, thermogravimetric (TG) curves of the magnetic wood were different from those of the natural wood and delignified wood. The mass loss in the temperature range of 210-340 °C was caused by the pyrolysis of wood components.^[29] More importantly, an extra decomposition step was observed starting at a temperature of approximately 600 °C, which corresponds to the reduction reaction between Fe₃O₄ and the char obtained from the pyrolysis of wood. [30] Notably, the weight of residues in the magnetic wood was 31.25 wt%, suggesting that the deposition of Fe₃O₄ minerals on the wood substrate was approximately 18.58 wt%. The differential thermal gravity (DTG) analysis was carried out, as shown in Figure 5d, wherein the obvious peaks of the magnetic wood and delignified wood were weakened compared with those of the natural wood, indicating a lower rate of total weight loss for the magnetic wood. This effect could be explained by the fact that the wood components were likely to be shielded by the inorganic Fe₃O₄ nanoparticles, which prevented the wood components from being accessible to oxygen and, thus, reduced the rate of combustion.

It is notable that the outstanding advantage of magnetic wood is its magnetic properties, which result in significantly enhanced EMI shielding performance. **Figure 6**b shows the magnetization

curves of magnetic wood measured using a vibrating sample magnetometer (VSM) at room temperature. As shown in Figure 6b, typical magnetic hysteresis behavior with a saturation magnetization of 4.5 emu g⁻¹ for the whole magnetic wood and a coercive field of 131.3 Oe was observed in the magnetic wood. However, the natural wood and delignified wood were observed to have typical diamagnetic behavior, as expected (Figure S7, Supporting Information). Currently, strong EMI shielding material is in high demand for electronic devices.^[3,6,31] Further EMI shielding tests were carried out using a network analyzer [phase network analyze (PNA), Agilent, E8364Al, a commercial ultrawide band (UWB) antenna, and a standard horn antenna. The detailed setup is shown in Figure 6a, where the UWB antenna was covered by different types of wood shields and the horn antenna was used to receive signals coming from the UWB antenna. All tests were conducted in an anechoic chamber to avoid electromagnetic noise from the environment. The s-parameter was then calculated within the PNA using the following equations

$$S_{11} = 10 \times \log_{10}(P_{1r}/P_1) \tag{1}$$

$$S_{21} = 10 \times \log_{10}(P_2/P_1) \tag{2}$$

where P_1 is the total power provided by the PNA, P_{1r} is the reflected power from the UWB antenna, and P_2 is the power received by the horn antenna.

Frequency sweeps from 5 to 12 GHz were used to identify the EMI shielding properties of natural wood, delignified wood, and magnetic wood, as shown in Figure S8, Supporting Information. The return loss curves (S_{11}) for natural wood and delignified

ENGINEERING MATERIALS

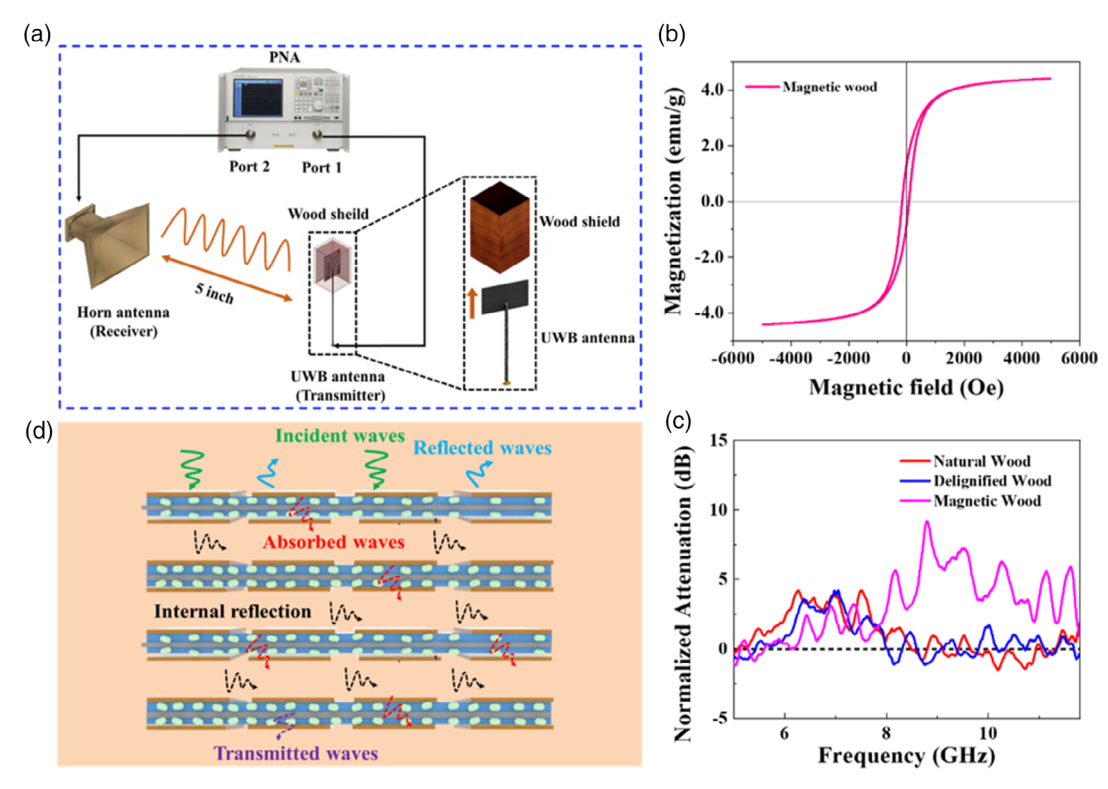


Figure 6. a) Schematic illustration of the setup for the EMI effectiveness measurement. b) The magnetization curves (magnetization versus magnetic field) of the magnetic wood samples at room temperature. c) Normalized S_{21} attenuation of natural wood, delignified wood, and magnetic wood. d) Schematic diagram of electromagnetic wave transfer across the magnetic wood, illustrating the EMI shielding mechanism.

wood show very stable patterns, as shown in Figure S8a, Supporting Information. Several spikes from delignified wood were observed due to its intrinsic material resonance. The use of the magnetic wood shield leads to a slight change in the S_{11} graph, which is mainly caused by the microwave signal reflection from magnetic wood. The transmission loss is presented in Figure S8b, Supporting Information, as S_{21} data. Substantially enhanced signal strength attenuation by 5-10 dB (or 7-10× enhancement) can be observed across the X-band (8-12 GHz) after applying the magnetic wood shield compared with the nonmagnetic wood shield. In conclusion, the substantial signal strength attenuation for magnetic wood indicates an excellent improvement in the EMI shielding effectiveness mainly due to the enhanced magnetic loss tangent of the magnetic wood compared with the nonmagnetic wood. As we presented in Table S1, Supporting Information, our work is comparable to reported values, but we are implementing our work on wood, which is nonconductive materials. The challenge is bigger, and we have more room for improvement.

The schematic diagram of the EMI shielding mechanism of magnetic wood is shown in Figure 6d. As electromagnetic incident waves contact the top surface, some waves are immediately reflected. The remaining waves pass through the wood interconnected porous network, where they interact with the Fe $_3$ O $_4$ nanoparticles deposited on the inner surface of the lumen walls in the wood, which results in electromagnetic wave attenuation due to the enhanced magnetic loss tangent of the magnetic wood. $^{[13,33]}$ Further improvements to the magnetic properties

may lead to enhance the EMI suppression capability. In addition, the mechanical properties of natural wood, delignified wood, and magnetic wood under the stretching process in the length direction are shown in Figure S9, Supporting Information. It can be found that the tensile stress-strain curves of three kinds of wood both show a linear deformation behavior before tensile failure. [8] The natural wood possesses the tensile strength of 30.15 MPa, which is ascribed to the hierarchical structure and the strong interactions among cellulose, hemicelluloses, and lignin. [24] Compared with the natural wood, the delignified wood possesses a tensile strength of 22.36 MPa due to the removal of lignin in the bleaching and cooking process. It is worth noting that the tensile strength of the magnetic wood (41.87 MPa) is 1.38 times higher than that of the natural wood and 1.86 times higher than that of the delignified wood, respectively. The superior mechanical property makes the magnetic wood desirable for structural materials application.

In summary, a ready process of alternating incubation cycles assisted by sonication impregnation was introduced to transport a ferric salt precursor into the mesoporous wood substrate, leading to magnetic wood. Magnetic Fe_3O_4 nanoparticles were deposited into the porous 3D structured organic wood scaffold by an in situ mineralization. Due to its natural mesoporous and interconnected porous network structure as well as enhanced magnetic loss tangent, excellent EMI shielding effectiveness was achieved in the 3 mm thick magnetic wood, which show an $\approx 7\text{--}10\times$ times improvement over its nonmagnetic counterpart, making the magnetic wood an attractive candidate as an

www.aem-journal.com

electromagnetic wave shielding material. Both the wood and iron element are abundant on Earth, and the fabrication process is environmentally friendly and scalable. Furthermore, the obtained magnetic wood is construable and much lighter than bulk magnetic metal. Attributed to the abovementioned merits, this novel magnetic wood is highly attractive for large-scale EMI shielding applications for buildings and electronics in space, military, and civil.

Experimental Section

Materials and Chemicals: Basswood was the wood featured in this work, and the dimension of the wood slices was 50 mm \times 80 mm with a thickness of 3 mm. The chemicals used for removing the lignin from the wood were NaOH (>98 wt%, Sigma-Aldrich), Na $_2$ SO $_3$ (98.5 wt%, Sigma-Aldrich), and H_2O_2 (30 wt% solution, Fisher Scientific). The chemicals used for impregnation to prepare the magnetic wood were FeSO $_4$ ·7H $_2$ O (MW = 278.01 g mol $^{-1}$, Fisher Scientific) and Na $_2$ CO $_3$ (MW = 105.99 g mol $^{-1}$, Fisher Scientific). The solvents used were ethanol (Fisher Scientific) and deionized (DI) water. All other chemicals were analytical grade and used as received without further purification.

Wood Delignification Treatment: In the cooking process, the wood slices were immersed in a solution, including NaOH (2.5 mol L $^{-1}$) and Na $_2$ SO $_3$ (0.4 mol L $^{-1}$) and boiled for 12 h. The slices were then rinsed in hot distilled water at least three times to remove most of the chemicals. $^{[8]}$ In the next bleaching process, the wood slices were then placed in the hot H $_2$ O $_2$ (3.0 mol L $^{-1}$) and boiled without stirring. When the yellow color of the wood sample disappeared, the wood sample was removed and rinsed with cold water. The lignin-removed wood slices were then preserved in ethanol. $^{[11]}$

Fabrication of Magnetic Wood: Nanosized Fe_3O_4 particles firmly attached to the inner surface of the wood cell walls by performing alternating incubation cycles with $FeSO_4$ and Na_2CO_3 solutions. An incubation cycle was defined as immersing the lignin-removed wood slice in $0.5 \, \text{mol L}^{-1} \, FeSO_4$ under agitation in a shaker for 24 h, sonication-assisted at least three times (10 min every time) to allow for in-depth diffusion into the porous wood structure, and then degased for 10 min to ensure full infiltration. The wood slice was then briefly rinsed in DI water and then transferred to $0.5 \, \text{mol L}^{-1} \, Na_2CO_3$ under agitation for another 24 h (sonication-assisted at least three times (10 min every time) to allow for indepth diffusion into the porous wood structure, and then degased for 10 min to ensure full infiltration). After being washed several times with DI water, the specimens were then dried in the oven while being pressed between two pieces of glasses at $60\,^{\circ}\text{C}$ for 24 h.

Characterization: SEM (S3700 Hitachi Ltd. Japan) was used to examine the morphology of the natural wood slices, delignified wood slices, and magnetic wood slices. The fixed samples were coated with a layer of approximately 30 Å thick gold. The accelerating voltage was 10 kV, and the working distance was 11 mm. For elemental analysis of wood samples, energy-dispersive X-ray spectroscopy (EDS) analysis was performed during SEM examination. The wood powder was deposited onto the KBr slice, and the FTIR spectra of the composite were recorded using a Nicolet FTIR 5700 spectrophotometer (Bruker, Germany) in transmission mode over the range of 500-4000 cm⁻¹ with a 4 cm⁻¹ resolution at 25 °C. XRD tests were conducted on an X-ray diffractometer (UI tima IV, Japan) using Cu kα radiation at 40 kV and 30 mA. The scan was from a two theta of 5° – 40° at a step size of 0.05° . [26] The thermal behavior of natural wood, delignified wood, and magnetic wood samples was measured using SDTQ600 (TA Instruments, USA) under nitrogen atmosphere from 40 to 800 °C at a heating rate of 10 °C min⁻¹. The XPS was measured in an AXIS UltraDLD (Shimadzu, Japan) using an Al Ka X-ray source and operating at 150 W. Each sample powder was dried in vacuo, and 10 mg was weighed for each sample. For mechanical test, the dimensions for tensile samples were approximately $50 \text{ mm} \times 10 \text{ mm} \times 3 \text{ mm}$. The samples were stretched along the sample length direction using the testing machine (Instron 5565) until they fractured with a constant test speed of $2~\text{mm}\,\text{min}^{-1}$ at room temperature. Magnetic properties of the three kinds of wood samples were characterized with a VSM (Lake shore 7400). The measurement of the magnetization versus the applied magnetic field was conducted at 300 K. The EMI shielding property test was carried out using a network analyzer (Agilent PNA E8364A), a commercial UWB antenna, and a standard horn antenna. The test samples were carefully cut into $22.86\times10.16~\text{mm}^2$ strips and assembled into a box.

Supporting Information

Supporting Information is available from the Wiley Online Library or from the author.

Acknowledgements

Z.C. and Y.W. contributed equally to this work. H. L. Zhu acknowledges financial support from Northeastern University and NSF-ECCS grant (1933051). The authors thank the Kostas Research Institute at Northeastern University for the use of their facilities. All the authors contributed to and commented on the manuscript.

Conflict of Interest

The authors declare no conflict of interest.

Keywords

construable, electromagnetic interference shielding, electromagnetic wave, inorganic mineralization, lightweight, magnetic wood

Received: March 2, 2020 Revised: May 28, 2020 Published online:

- C. Liang, P. Song, H. Qiu, Y. Zhang, X. Ma, F. Qi, H. Gu, J. Kong, D. Cao, J. Gu, *Nanoscale* **2019**, *11*, 22590.
- [2] H. Lv, X. Liang, G. Ji, H. Zhang, Y. Du, ACS Appl. Mater. Interfaces 2015, 7, 9776.
- [3] Z. Lou, H. Han, M. Zhou, J. Han, J. Cai, C. Huang, J. Zou, X. Zhou, H. Zhou, Z. Sun, ACS Sustain. Chem. Eng. 2017, 6, 1000.
- [4] a) H. Wu, G. Wu, Y. Ren, L. Yang, L. Wang, X. Li, J. Mater. Chem. C 2015, 3, 7677; b) W. Gan, L. Gao, X. Zhan, J. Li, RSC Adv. 2015, 5, 45919; c) C. Liang, P. Song, H. Qiu, Y. Huangfu, Y. Lu, L. Wang, J. Kong, J. Gu, Composit. A Appl. Sci. Manufact. 2019, 124, 105512.
- [5] Z. Lou, Y. Li, H. Han, H. Ma, L. Wang, J. Cai, L. Yang, C. Yuan, J. Zou, ACS Sustain. Chem. Eng. 2018, 6, 15598.
- [6] N. Li, Y. Huang, F. Du, X. He, X. Lin, H. Gao, Y. Ma, F. Li, Y. Chen, P. C. Eklund, *Nano Lett.* **2006**, *6*, 1141.
- [7] Y. Yang, M. C. Gupta, K. L. Dudley, R. W. Lawrence, Adv. Mater. 2005, 17, 1999.
- [8] J. Song, C. Chen, S. Zhu, M. Zhu, J. Dai, U. Ray, Y. Li, Y. Kuang, Y. Li, N. Quispe, *Nature* 2018, 554, 224.
- [9] C. Chen, S. Xu, Y. Kuang, W. Gan, J. Song, G. Chen, G. Pastel, B. Liu, Y. Li, H. Huang, Adv. Energy Mater. 2019, 9, 1802964.
- [10] F. Jiang, T. Li, Y. Li, Y. Zhang, A. Gong, J. Dai, E. Hitz, W. Luo, L. Hu, Adv. Mater. 2018, 30, 1703453.
- [11] M. Zhu, J. Song, T. Li, A. Gong, Y. Wang, J. Dai, Y. Yao, W. Luo, D. Henderson, L. Hu, Adv. Mater. 2016, 28, 5181.
- [12] Z.-L. Yu, N. Yang, L.-C. Zhou, Z.-Y. Ma, Y.-B. Zhu, Y.-Y. Lu, B. Qin, W.-Y. Xing, T. Ma, S.-C. Li, Sci. Adv. 2018, 4, eaat7223.



www.aem-journal.com

- [13] Y. Yuan, X. Sun, M. Yang, F. Xu, Z. Lin, X. Zhao, Y. Ding, J. Li, W. Yin, Q. Peng, ACS Appl. Mater. Interfaces 2017, 9, 21371.
- [14] M. Yeniocak, O. Goktas, M. Colak, E. Ozen, M. Ugurlu, Maderas. Ciencia y tecnología 2015, 17, 711.
- [15] a) D. Hradil, T. Grygar, J. Hradilová, P. Bezdička, Appl. Clay Sci. 2003, 22, 223; b) N. Guskos, G. Papadopoulos, V. Likodimos, S. Patapis, D. Yarmis, A. Przepiera, K. Przepiera, J. Majszczyk, J. Typek, M. Wabia, Mater. Res. Bull. 2002, 37, 1051; c) N. Guskos, G. Papadopoulos, V. Likodimos, S. Patapis, D. Yarmis, A. Przepiera, K. Przepiera, J. Majszczyk, J. Typek, M. Wabia, Mater. Res. Bull. 2002, 37, 1051; d) T. Grygar, P. Bezdička, D. Hradil, A. Doménech-Carbó, F. Marken, L. Pikna, G. Cepriá, Analyst 2002, 127, 1100.
- [16] V. Merk, M. Chanana, S. Gaan, I. Burgert, Holzforschung 2016, 70, 867.
- [17] a) G. Mustoe, M. Acosta, Geosciences 2016, 6, 25; b) L. Roberts, J. Geol. 1940, 48, 212.
- [18] H. Guan, Z. Cheng, X. Wang, ACS Nano 2018, 12, 10365.
- [19] Y. Wu, J. Wu, F. Yang, C. Tang, Q. Huang, Polymers 2019, 11, 776.
- [20] a) E. Vasileva, Y. Li, I. Sychugov, M. Mensi, L. Berglund, S. Popov, Adv. Opt. Mater. 2017, 5, 1700057; b) Y. Li, S. Yu, J. G. Veinot, J. Linnros, L. Berglund, I. Sychugov, Adv. Opt. Mater. 2017, 5, 1600834.
- [21] V. Merk, M. Chanana, N. Gierlinger, A. M. Hirt, I. Burgert, ACS Appl. Mater. Interfaces 2014, 6, 9760.
- [22] Y. Huang, Y. Chen, X. Fan, N. Luo, S. Zhou, S. C. Chen, N. Zhao, C. P. Wong, Small 2018, 14, 1801520.

- [23] U. Jeong, X. Teng, Y. Wang, H. Yang, Y. Xia, Adv. Mater. 2007, 19, 33.
- [24] W. Gan, L. Gao, S. Xiao, W. Zhang, X. Zhan, J. Li, J. Mater. Sci. 2017, 52, 3321.
- [25] N. Gierlinger, L. Goswami, M. Schmidt, I. Burgert, C. Coutand, T. Rogge, M. Schwanninger, *Biomacromol.* 2008, 9, 2194.
- [26] Z. Cheng, H. Ye, F. Cheng, H. Li, Y. Ma, Q. Zhang, A. Natan, A. Mukhopadhyay, Y. Jiao, Y. Li, Adv. Mater. Interfaces 2019, 6, 1802010.
- [27] M. Ma, Y. Zhang, W. Yu, H.-y. Shen, H.-q. Zhang, N. Gu, Colloids Surfaces A Physicochem. Eng. Aspects 2003, 212, 219.
- [28] W. Gan, L. Gao, S. Xiao, R. Gao, W. Zhang, J. Li, X. Zhan, Adv. Mater. Interfaces 2017, 4, 1700777.
- [29] B. Hu, C. Zhao, X. Jin, H. Wang, J. Xiong, J. Tan, Colloids Surfaces A: Phys. Eng. Aspects 2015, 484, 278.
- [30] C. Wan, J. Li, ACS Sustain. Chem. Eng. 2015, 3, 2142.
- [31] F. Shahzad, M. Alhabeb, C. B. Hatter, B. Anasori, S. M. Hong, C. M. Koo, Y. Gogotsi, *Science* 2016, 353, 1137.
- [32] Y. Chen, H. B. Zhang, Y. Yang, M. Wang, A. Cao, Z. Z. Yu, Adv. Funct. Mater. 2016, 26, 447.
- [33] Y. Wu, Z. Wang, X. Liu, X. Shen, Q. Zheng, Q. Xue, J.-K. Kim, ACS Appl. Mater. Interfaces 2017, 9, 9059.
- [34] J. S. Segmehl, A. Laromaine, T. Keplinger, A. May-Masnou, I. Burgert, A. Roig, J. Mater. Chem. C 2018, 6, 3395.